Applied Soft Computing Journal 186 (2026) 114087

Contents lists available at ScienceDirect

Applied Soft Computing

journal homepage: www.elsevier.com/locate/asoc

EEG-based Parkinson's disease classification method by integrating topological features and multi-scale spatio-temporal networks

Weixiang Gao[a], Yunyuan Gao[a], Jiangwen Lu[a], Xugang Xi[a], Xiaohui Lou[b,c,*]

[a] College of Automation, Hangzhou Dianzi University, Hangzhou, China
[b] Rui'an People's Hospital, Wenzhou, China
[c] The Third Affiliated Hospital of Wenzhou Medical University, Wenzhou, China

HIGHLIGHTS

- This paper innovatively proposes an electrode topology rearrangement-based spatial reorganization method, enhancing EEG spatial information encoding through electrode sequence optimization.
- In this paper, a hybrid architecture combining multi-scale spatial convolution with temporal periodic decomposition network (STTCNN) is developed. It achieves dynamic feature interactions through LSTM-mediated spatio-temporal integration to address the problem of under-modeling spatio-temporal feature coupling in EEG.
- Comprehensive evaluations on public PD Oddball datasets demonstrate the proposed STTCNN model's superior performance. The model outperforms state-of-the-art baselines, as shown through comparative and ablation studies.

GRAPHICAL ABSTRACT

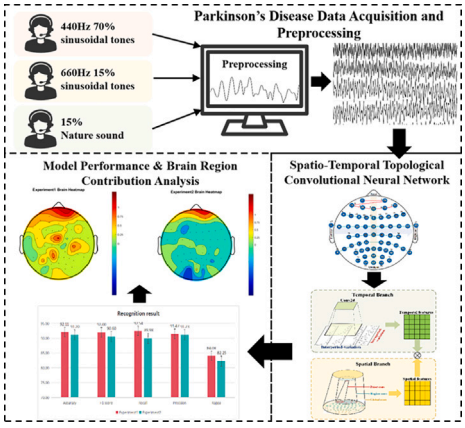

ARTICLE INFO

Keywords:
EEG
Parkinson's disease
Spatio-temporal features
TimesNet
Convolutional neural networks

ABSTRACT

As a highly prevalent neurodegenerative disease, early diagnosis of Parkinson's disease (PD) is essential for delaying disease progression and improving patients' quality of life. EEG-based deep learning methods have the core advantages of non-invasiveness, low cost, and early diagnostic power. However, existing studies face the issue that the extracted feature types are too limited, resulting in the failure to fully integrate and extract spatio-temporal dynamic information, which makes the model recognition performance limited. To address these issues, this study combines the electrode topology mechanism with the cycle sensitivity of TimesNet and the optimized progressive spatial convolution method to propose a novel spatio-temporal topological convolutional neural network (STTCNN). Firstly, the electrode topology mechanism is designed to enhance the EEG spatial characterization by modeling the spatial distribution of scalp electrodes. Secondly, the progressive spatial convolution is employed to extract multi-scale spatial features, which synergistically combines with TimesNet to comprehensively

* Corresponding author at: Rui'an People's Hospital, Wenzhou, China.
Email address: louxiaohui@163.com; gyy@hdu.edu.cn (X. Lou).

https://doi.org/10.1016/j.asoc.2025.114087
Received 30 April 2025; Received in revised form 6 September 2025; Accepted 7 October 2025
Available online 30 October 2025

explore both periodic and non-stationary patterns within EEG time series. Ultimately, the long-term and short-term temporal dependencies are integrated through LSTM to formulate the classification decision framework for Parkinson's Disease detection. The model was extensively tested on public datasets, demonstrating significant performance improvements over existing baseline methods with key performance metrics of Accuracy 92.11 %, F1-score 92.00 %, Recall 92.54 %, Precision 91.47 %, and Kappa coefficient 84.08 %. This paper innovatively constructs a framework for collaborative EEG spatio-temporal feature extraction. It not only verifies specific EEG activity patterns in Parkinson's patients but also provides a highly interpretable and generalizable method for developing clinical auxiliary diagnostic tools.

1. Introduction

Parkinson's disease (PD) is a chronic neurodegenerative disorder. It is primarily caused by dopaminergic neuronal degeneration in the substantia nigra [1]. PD manifests cardinal motor symptoms including bradykinesia, tremor, and rigidity [2,3]. It frequently coexists with non-motor manifestations such as cognitive impairment, depression, and sleep disturbances [4,5].

In clinical diagnostics, Parkinson's disease (PD) is conventionally assessed through clinical manifestations [6]. However, traditional scale-based approaches suffer from inherent subjectivity and limited capacity for early-stage change detection [7]. Non-motor symptoms, though frequently overlooked, profoundly impact patients' quality of life and may emerge at any stage of the disease [8]. Physiological signal-based methodologies utilizing electroencephalography (EEG), magnetoencephalography (MEG) [9], and neuroimaging techniques including magnetic resonance imaging (MRI) [10] and functional magnetic resonance imaging (fMRI) [11], objectively reflect structural and functional alterations in cerebral networks. These provide more precise foundations for early diagnosis and pathophysiological investigations. Among these, EEG demonstrates unique advantages in elucidating dynamic cortical information processing characteristics in PD patients through millisecond-level temporal resolution and operational practicality [12,13]. In addition, EEG studies employing auditory Oddball paradigms have further transcended traditional cognitive assessment limitations. This paradigm facilitates the dynamic trajectory reconstruction of prodromal executive dysfunction through neural oscillation pattern analysis associated with attentional allocation and cognitive control [14,15], establishing critical foundations for developing PD-specific neural biomarkers.

In EEG-based PD detection research, several important research directions have emerged for exploring brain network features: On one hand, the value of multi-scale analysis in capturing the hierarchical structure of brain networks affected by PD has been widely recognized. Qiu et al. (2022) [16] developed a multi-scale convolutional neural network (MCNN), which integrates power spectral density (PSD) and phase-locked value (PLV) features across multiple frequency bands to identify healthy controls and PD patients. Additionally, other studies have extracted multi-scale fuzzy entropy (MSFEn) features from EEG signals to quantify the complexity and irregularity of EEG signals across different temporal scales, providing a new perspective for analyzing PD-related abnormal neural electrical activities [17]. On the other hand, spatial association analysis has revealed key insights into alterations in the organization of brain networks in PD patients. Among various approaches, microstate-based methods have shown outstanding performance: they can effectively characterize the spatio-temporal variability of dynamic functional connectivity networks and provide crucial support for analyzing abnormal brain network patterns in early-stage PD [18].

Despite the incremental progress in EEG-based Parkinson's disease detection research, existing methods still face significant challenges in joint spatio-temporal feature modeling [19]. In terms of temporal feature research, current studies often focus on EEG continuity and frequency domain characteristic analysis [20,21] or extract variation information between adjacent time points through one-dimensional convolution operations in the time dimension [22]. However, these methods are limited by the locality of one-dimensional convolution kernels and the complex non-stationary characteristics of time series, which restrict their ability to explore long-term dependencies of complex temporal patterns [23]. The introduction of TimesNet [24] provides a new approach. It decomposes periodic fluctuations of time series into refined representations within periods (intraperiod) and between periods (interperiod), offering a new paradigm for time series modeling. Nevertheless, its single-dimensional temporal analysis framework struggles to comprehensively capture the spatial topological information embedded in EEG signals. Regarding spatial feature modeling, existing research mainly adopts two methods. The first approach employs graph-based modeling methods, using electrodes as graph nodes to construct brain connectivity networks [25–27]. Spatial topological characteristics are represented through connection relationships between nodes. The second approach involves the extraction of predefined features, such as time–frequency features and nonlinear indicators, and embedding them into electrode channels [28,29] to achieve multi-dimensional feature fusion.

Although these methods have shown potential in Parkinson's detection, key issues remain. First, graph structure modeling typically defines nodes only at the single electrode scale. This ignores the multi-scale characteristics of brain functional networks, such as the synergy between local brain regions and global networks. Second, feature embedding strategies can enrich semantic information in the channel dimension but fail to explicitly model spatial association patterns across channels. Additionally, despite attempts to extract deep features by combining electrode spatial distribution [30], the analysis of dynamic functional coupling mechanisms between brain regions and topological association characteristics remains insufficient.

To address these issues, this study proposes an innovative framework that integrates electrode topology rearrangement with multi-scale spatio-temporal feature learning. The scalp spatial topological relationship is reconstructed by the electrode sequence rearrangement mechanism, combined with TimesNet—chosen for its superior multi-scale periodic pattern recognition capabilities over Transformer approaches and computational efficiency for long EEG sequences—to achieve cycle-sensitive temporal modeling. Progressive spatial convolution is introduced to extract hierarchical spatial features capturing local-global network synergies. Finally, the dynamic coupling of spatio-temporal features is achieved by Long Short-Term Memory (LSTM), selected over GRU and attention-based models for its superior long-term dependency modeling and proven effectiveness in capturing dynamic functional coupling mechanisms in biomedical signals [31]. The method improves the spatial characterization of EEG data, captures the inter-periodic and intra-periodic variations of the time series, and significantly improves the accuracy of the PD classification task through multi-scale feature extraction and fusion.

(1) To address the insufficient EEG spatial topology characterization, this paper innovatively proposes a spatial reorganization method based on electrode topological alignment by reorganizing electrode sequences to enhance the encoding of EEG spatial information.
(2) In response to the problem of insufficient modeling of EEG spatio-temporal feature coupling, the paper develops a hybrid architecture, which combines multi-scale spatial convolution

with temporal periodicity decomposition networks, called Spatio-Temporal Topological Convolutional Neural Network (STTCNN). It achieves dynamic feature interaction through LSTM-mediated spatio-temporal integration.

(3) Comprehensive evaluations on public PD auditory Oddball datasets demonstrate the proposed STTCNN model's superior performance. The model outperforms state-of-the-art baselines, as shown through comparative and ablation studies.

2. Material and processing

2.1. PD database and preprocessing engineering

The PD auditory Oddball dataset [32] consists of 50 participants, including 25 Parkinson's disease patients (PD group) and 25 gender and age matched healthy controls (control group, CTL). In the experimental protocol, each PD patient underwent testing in both medication state (ON, post-dosing) and medication-withdrawn state (OFF, 15-hour withdrawal), with one-week intervals between sessions. The initial experimental sequence assigned 13 participants to the ON state and 12 to the OFF state, with all testing commencing at 9:00 AM. Neuropsychological evaluations and questionnaire assessments were exclusively conducted in the ON state. Motor symptoms in PD patients, quantified using the Unified Parkinson's Disease Rating Scale (UPDRS), were video-recorded during each session and subsequently evaluated by neurologists. All participants demonstrated Mini Mental State Exam (MMSE) scores exceeding 26, indicating preserved cognitive functioning within normal ranges. No significant differences were observed between PD and control groups in educational background or premorbid intelligence levels (see Table 1).

Detailed data are presented in the Appendix A, including gender, age, and well-matched PD-CTL pair IDs. According to matching criteria, a total of 24 matched subject pairs were included, consisting of 24 PD patients and 24 healthy controls.

The acoustic stimuli comprised standard stimuli (440 Hz sine waves at 80 dB, 70 % trial frequency), target stimuli (660 Hz sine waves at 80 dB, 15 % trial frequency), and novel distractors (natural sounds averaging 65 dB, 15 % trial frequency), each with 200 ms duration.

Considering that EEG signals may be affected by various noises during acquisition, the MATLAB EEGLAB toolbox was used for preprocessing to eliminate these influences. Initially, band-pass filtering was applied to all electroencephalographic signals using a Butterworth filter with cutoff frequencies of 0.5–49 Hz (filter order: 2, zero-phase filtering). Notch filtering at 60 Hz with a bandwidth of 1 Hz was used to remove power frequency interference. Due to signal unreliability, electrodes near the ventral temporal lobe and some unusable electrodes were removed, reducing the original 64 electrodes to 60. The signals were epoched around stimulus onset (-2000 to 2000 ms) to isolate relevant stimulus responses. The activity of reference electrode CPz was recreated, bad channels and epochs were identified, and eye blinks were eliminated using the FASTER algorithm [33](channel correlation threshold: 0.4, variance threshold: 3 SD). Independent Component Analysis (ICA) was employed using the extended Infomax algorithm to remove eye blinks [components were rejected based on: correlation with EOG channels > 0.9, frontal topography, and temporal activation patterns consistent with ocular artifacts]. Downsampling to 128 Hz was performed to improve the signal-to-noise ratio. Subsequently, the data were re-referenced to the average reference. The paper extracted 1000–1500 ms from each trial and labeled all trials from PD patients as 1 and those from the control group (CTL) as 0.

Table 1
Patient and control participant demographics (mean ± SD).

parameters	PD(N = 24)	HC(N = 24)	P-value(*t*-test)
Sex	15 M, 9 F	15 M, 9 F	1.000
Age	69.75(8.91)	69(9.78)	0.770
MMSE	28.68 (1.03)	28.76(1.05)	0.791
UPDRS ON	23.36 (9.87)		
UPDRS OFF	24.80 (8.66)		

3. Method

The architecture of the Spatio-Temporal Topological Convolutional Neural Network (STTCNN) model proposed in this research is illustrated in Fig. 1.

Initially, the original EEG data is reconstructed using electrode topological reorganization to enhance the spatial representation of EEG. Subsequently, the reorganized EEG signals after electrode topological permutation are input into the feature extraction module, which implements multi-scale spatio-temporal feature learning through a dual-branch architecture. In the temporal dimension, a multi-scale temporal periodic decomposition network extracts time-varying rhythmic features; in the spatial dimension, a progressive spatial convolutional network captures multi-scale spatial representations. Finally, the dynamic interaction of spatio-temporal features is achieved through a feature fusion layer, which is then input to an LSTM network [31] for spatio-temporal feature modeling, ultimately completing the classification task through joint spatio-temporal representation.

3.1. Topological rearrangement of electrodes

To address the limitations in existing EEG topological representations, which include insufficient modeling of multi-scale dynamic characteristics and missing functional connectivity encoding, this paper innovatively proposes an electrode topological reorganization method, as shown in Fig. 2.

The core idea is to transform the standard 2D electrode layout into a sequence that better reflects brain anatomy and functional relationships. Instead of using arbitrary electrode ordering, the paper reorganizes electrodes based on their actual spatial positions on the head. The pseudo-code of the algorithm is as follows:

Algorithm 1 Electrode topological rearrangement.

Require: Original electrode positions $E = \{e_1, e_2, \ldots, e_{60}\}$
Ensure: Reorganized electrode sequence $S = \{s_1, s_2, \ldots, s_{60}\}$
Initialize reference points:
nasion_point ← get_nasion_coordinate()
inion_point ← get_inion_coordinate()
$left\_ear$ ← get_left_auricular_coordinate()
right_ear ← get_right_auricular_coordinate()
Initialize empty sequence $S \leftarrow \emptyset$
for each *sagittal_level* from *nasion_point* to *inion_point* **do**
  electrodes_at_level ← get_electrodes_at_sagittal_level (*sagittal_level*)
  Sort *electrodes_at_level* from $left\_ear$ to *right_ear*
  for each *electrode* in *electrodes_at_level* **do**
    Append *electrode* to sequence S
  end for
end for
Create topological mapping:
topology_matrix ← reshape(S, *rows* = *sagittal_divisions*, *cols* = *coronal_divisions*)
return reorganized electrode sequence S

Based on the standard EEG electrode coordinate system, this method enhances the representational capability of brain region correlation features by introducing a spatial topological reorganization mechanism, resulting in electrode sequences with different topological properties.

Specifically, four directional reference points are established based on neuroanatomical prior knowledge: the Nasion as the anterior reference, the left and right Auricular points as horizontal references,

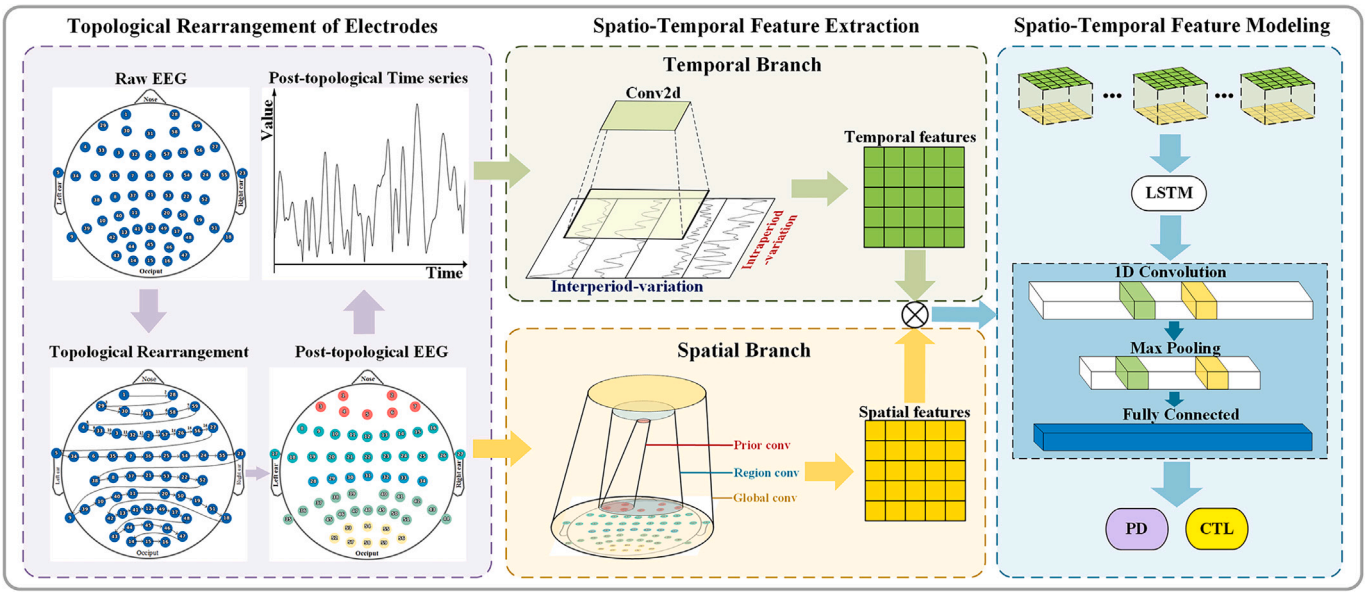

Fig. 1. Spatio-Temporal feature fusion-based EEG model for Parkinson's disease detection.

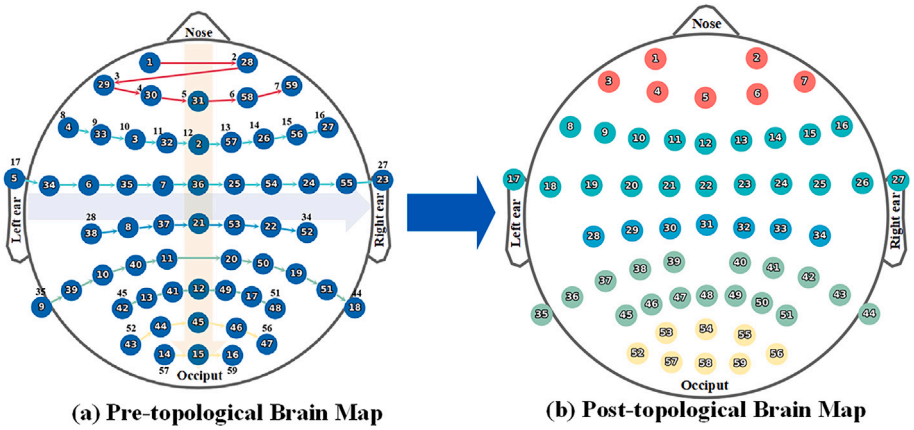

Fig. 2. Topology reorganization rules: (a) The blue circles in the figure indicate the electrode sequence numbers before topology arrangement, and the numbers on the arrows represent the electrode sequence numbers after topology arrangement. (b) shows the topology-arranged brain map.

and the Inion as the posterior anchor point, establishing a three-dimensional head model coordinate system [30]. Within this framework, the paper innovatively proposes a horizontally-prioritized electrode rearrangement strategy as shown in Fig. 2. Electrode numbering extends longitudinally along the sagittal axis from the Nasion to the Inion, following a horizontal sequence arrangement from left ear to right ear, ultimately forming a spatial reorganization matrix covering the 60-lead system. This arrangement offers dual advantages. First, through anatomically-driven topological mapping, it explicitly encodes the spatial distances between electrodes and functional associations of brain regions; second, the hierarchical arrangement structure provides an interpretable feature aggregation path for subsequent progressive spatial convolution. Fig. 2 uses a color-coded strategy to visually identify the functional regions of the brain.

3.2. Spatio-temporal topological convolutional neural network

The STTCNN model is primarily divided into a spatio-temporal feature extraction section (temporal branch and spatial branch) and a spatio-temporal feature fusion modeling (LSTM) section. The temporal branch utilizes TimesNet to decompose complex temporal variations into two-dimensional tensors containing intraperiod-variations and interperiod-variations, thereby capturing fine-grained temporal domain features of EEG. The spatial branch first reconstructs the ordered EEG information using a graph structure, then applies three convolutional blocks to perform convolution at three scales—electrode, brain region, and whole brain—thus obtaining multi-scale spatial features of EEG. Finally, the temporal and spatial features are mapped and fused through element-wise multiplication before being input into an LSTM for classification.

3.2.1. Temporal branch

The core architecture of the temporal branch is based on the TimesNet model, which effectively captures two key temporal patterns at each time point across multiple periodic dimensions through multi-period temporal modeling: fine-grained intraperiod-variations and macro-evolutionary patterns across periods interperiod-variations, as shown in Fig. 3.

This model overcomes the limitations of traditional one-dimensional structures that can only represent correlations between adjacent time points by converting one-dimensional time series into multi-period 2D tensors. First, the EEG data $X_{1D} \in R^{T \times C}$ after topological reorganization

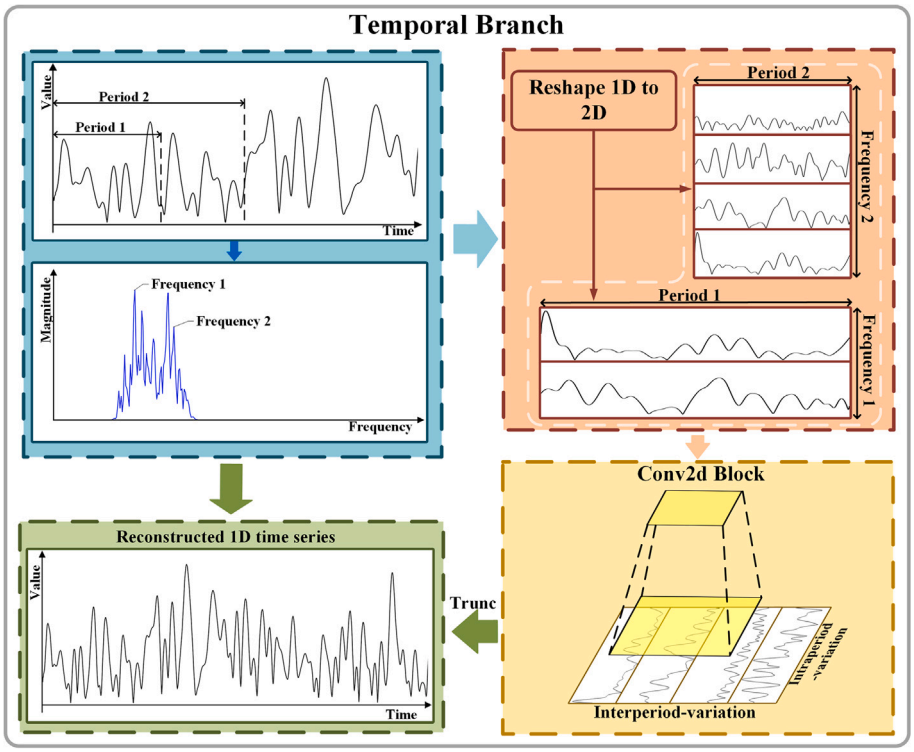

Fig. 3. Temporal branch process.

is used as input for dimensional transformation, where T - represents the number of time points and C - represents the number of reorganized electrodes. The method for converting 1D tensor to 2D tensor can be defined as:

$$A = Avg(Amp(FFT(X_{1D}))) \tag{1}$$

$$\{f_1, \ldots, f_k\} = \underset{f \in \{1,\ldots,\left\lfloor \frac{T}{2} \right\rfloor\}}{argTopk}(A) \tag{2}$$

$$p_i = \left\lceil \frac{T}{f_i} \right\rceil, i \in \{1, \ldots, k\} \tag{3}$$

where FFT(·) and Amp(·) - denote Fast Fourier Transform and amplitude computation; $A \in R^T$ - represents frequency-wise amplitudes averaged across channels via Avg(·). To mitigate spectral noise from insignificant high frequencies [34,35], we selectively retain top-k amplitudes $\{A_{f1}, \ldots, A_{fk}\}$ corresponding to dominant frequencies $\{f_1, \ldots, f_k\}$ (k being a hyperparameter), each associated with period lengths $\{p_1, \ldots, p_k\}$. Given frequency domain conjugate symmetry, only frequencies within $\{1, \ldots, \left\lceil \frac{T}{2} \right\rceil\}$ are considered. Consequently, the time series is restructured into 2D tensors encapsulating multi-periodic dynamics:

$$X^i_{2D} = Reshape_{p_i, f_1}(Padding(X_{1D})), i \in \{1, \ldots, k\} \tag{4}$$

where Padding(·) - applies zero-padding along the temporal axis to enable reshaping into $p_i * f_i$ dimensions (p_i: rows, f_i: columns). Notably, $X^i_{2D} \in R^{p_i \times f_i \times C}$ represents the i-th reconstructed 2D tensor derived from frequency f_i, with columns encoding intraperiod-variations and rows characterizing interperiod-variations under period length p_i. The final output comprises a set of 2D tensors $\{X^1_{2D}, \ldots, X^k_{2D}\}$ encapsulating k distinct periodic-induced temporal representations.

After converting 1D tensors to 2D tensors, multiple 2D convolutional kernels are employed to capture complex temporal information within these 2D tensors, with adaptive aggregation of representations from different time periods in the final stage. This process can be formalized as follows:

$$X^i_{1D} = Trunc(Reshape_{1, pi \times fi}(CNN(X^i_{2D}))), i \in \{1, \ldots, k\} \tag{5}$$

where the CNN(·) operation incorporates multiple 2D convolutional kernels to extract complex temporal features from these 2D tensors. Since different periods result in 2D tensors of varying shapes, this paper employs convolutional kernels of uniform size across the CNN Block to enable parameter sharing and improve feature extraction efficiency across different periods. The key advantage of applying 2D convolution to these reshaped tensors lies in its ability to simultaneously capture both intra-period variations (along columns) and inter-period variations (along rows), enabling comprehensive multi-periodic temporal modeling that traditional 1D convolution cannot achieve. Subsequently, to enable fusion with spatial features in later stages, the 2D tensors are transformed back into 1D space using the Trunc(·) operator that truncates padded sequences of length $(p_i \times f_i)$ to restore the original temporal length T.

Finally, since the amplitude A reflects the relative significance of selected frequencies and periods [36], we leverage corresponding amplitudes to aggregate 1D representations, producing the temporal branch's final output through the following computation:

$$X'_{1D} = \sum_{i=1}^{k} Softmax(A_i) \times X^i_{1D} \tag{6}$$

where × - is the Hadamard product.

3.2.2. Spatial branch

To fully capture deep spatial features from EEG data, the spatial branch adopts a progressive feature extraction method as shown in Fig. 4.

The spatial branching consists mainly of three different convolutional blocks progressively extracting multiscale spatial features of the topologized post-electroencephalographic data. Firstly, in the prior convolutional block, a directed weighted graph $G = \{V, E, A\}$ is obtained by modeling the EEG signals from EEG signals $x_{1D} \in R^{T \times C}$, where $\{V_i\}^C_{i=1}$ -

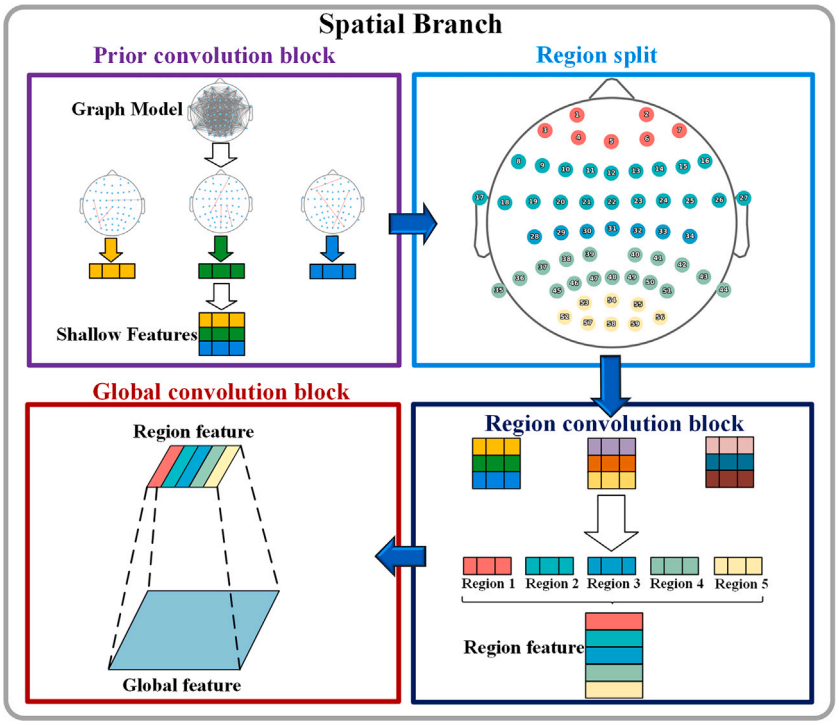

Fig. 4. Spatial branch process.

represents electrode nodes; E - denotes edges weighted by inter-electrode correlations; $A \in R^{C\times C}$ - represents the dynamic adjacency matrix generated according to the correlation between electrodes, defined as follows:

$$A = \begin{cases} 1 & \text{if } |R_{i,j}| > threshold (i \neq j) \\ 0 & other \end{cases} \tag{7}$$

where $R_{i,j}$ - is the correlation coefficient generated based on the covariance between channels. The correlation threshold for generating the adjacency matrix is set to 0.3, which is determined to be slightly larger than the minimum correlation value among all electrode pairs [37]. This threshold selection ensures that only meaningful inter-electrode correlations contribute to the graph structure while effectively filtering out weak or spurious connections that may introduce noise into the spatial topology representation. On this basis, two layers of graph convolution are applied to extract the shallow spatial features of the EEG, providing an important foundation for the subsequent progressive feature extraction. The graph convolution calculation process is as follows:

$$\dot{A} = D^{-\frac{1}{2}} A D^{\frac{1}{2}} \tag{8}$$

$$S = g(X_{1D}, \dot{A}) \tag{9}$$

where D - is degree matrix; $\dot{A} \in R^{C\times C}$ - refers to the normalized adjacency matrix; $S \in R^{T\times C}$ - represents the shallow spatial features obtained after graph convolution.

Then, in the brain region convolution block, based on the spatial distribution of the electrodes and their association with the functional regions of the brain, the shallow spatial features are divided into five brain regions, as shown in Fig. 2. Each brain region undergoes independent convolution operations to extract local spatial patterns between electrodes within the region, defined as follows:

$$S'_i = Region\ conv(S), i \in \{1, \dots 5\} \tag{10}$$

where Region conv(·) - represents the region convolution block; S'_i - indicates localized features of each brain region after the convolution of brain regions.

Subsequently, the features from each brain region are concatenated along the electrode dimension and then processed through global convolution to achieve progressive spatial feature extraction:

$$S'_{1D} = Global\ conv(Concatenate(S'_i)), \quad i \in \{1, \dots, 5\} \tag{11}$$

where S'_i - represents the features from the i-th brain region; and $S'_{1D} \in R^{T\times C}$ - denotes the final global spatial features. This progressive convolution strategy effectively integrates interaction information between different brain regions, transitioning from local regional features to comprehensive whole-brain representations.

3.2.3. Spatio-temporal feature modeling

To fully utilize both temporal and spatial features, element-wise multiplication is applied to fuse the temporal and spatial features, followed by LSTM networks to model temporal dynamics. The complete process is defined as follows:

$$\dot{F} = LSTM(X'_{1D} \times S'_{1D}) \tag{12}$$

where $X'_{1D} \in R^{T\times C}$ - denotes temporal features; $S'_{1D} \in R^{T\times C}$ - represents spatial features; and $\dot{F}$ - denotes the final spatio-temporal representations. This fusion mechanism not only facilitates the linear recombination of spatio-temporal patterns in high-dimensional spaces to capture intricate nonlinear relationships through element-wise multiplication, but also enables comprehensive temporal dynamics modeling via LSTM networks, yielding optimally fused spatio-temporal representations with enhanced feature utilization efficiency.

Subsequently, the processed spatio-temporal representations $\dot{F}$ are fed into fully-connected layers to generate output, formally defined as:

$$Output = Linear(Maxpooling(Conv(\dot{F}))) \tag{13}$$

where Conv(·) - denotes a layer of 1D convolution, which helps reduce redundant information and adjust the shape of the feature map after LSTM processing; Maxpooling(·) - reduces the model complexity by decreasing the feature dimensions during the training process, thereby

avoiding overdependence on the training data and improving the generalization ability of the model; Linear(·) - denotes the fully connected layer, which performs a transformation of dimensionality reduction through a trainable weight matrix to obtain final predictions.

3.3. Optimization of STTCNN

Upon model architecture completion, the critical challenge of parameter optimization for loss function minimization requires systematic resolution. In this investigation, the model employs the Adam optimizer for parameter refinement, formally defined as:

$$optimizer = Adam(para, lr, decay) \tag{14}$$

This optimizer combines momentum optimization and adaptive learning rate techniques, accelerating the training process and improving the model's convergence. The learning rate (lr) is dynamically adjusted multiple times, with the final value set to 0.0001. This value is chosen to ensure a thorough optimization process while preventing oscillations or divergence during the early stages of training. Additionally, the weight decay coefficient (wd) is set to 0.0001, which controls the model's regularization strength, preventing overfitting and enhancing generalization ability. For the loss function, cross-entropy is adopted as the optimization objective:

$$L = -\frac{1}{N}\sum_{i=1}^{N}\sum_{c=1}^{C} y_{i,c} \cdot log(p_{i,c}) \tag{15}$$

where N - is sample size; C - denotes number of classes; $y_{i,c}$ - represents the true label of the i-th sample; and $p_{i,c}$ - denotes predicted probability that the i-th sample belongs to category c. This is a loss function commonly used for classification problems, which measures the difference between the predicted probability distribution and the actual label's probability distribution, aiming to guide the model in producing more accurate predictions.

In summary, the model gradually optimizes its performance during the training process. By selecting the optimizer and loss function, it effectively addresses the optimization issues in the learning process.

3.4. Evaluation index and experimental settings

To comprehensively evaluate the model's performance, we employed standard classification metrics including Accuracy, Precision, Recall, F1-score, and Cohen's Kappa coefficient [38]. The confusion matrix for binary classification (PD vs. Control) is defined in Table 2, where TP, TN, FP, and FN represent true positives, true negatives, false positives, and false negatives, respectively.

Accuracy serves as the primary evaluation metric, representing the proportion of correctly classified samples. The F1-score provides a balanced measure of Precision and Recall performance. Cohen's Kappa coefficient eliminates random agreement bias and provides a more robust assessment of classification consistency beyond simple accuracy.

The relevant parameter settings during model training are specified as follows. The EEG electrode count C corresponds to 60 channels after excluding artifact-contaminated electrodes from the original database. Both temporal and spatial branches output feature matrices with a dimensionality of 64. For the hyperparameter K (number of dominant periodic components in the temporal branch), the paper sets K = 2 following the TimesNet methodology, where top-k frequencies are selected based on FFT amplitudes, allowing the model to focus on the two most dominant periodic patterns while balancing computational efficiency with temporal modeling capability [24]. The learning rate selection was validated through comparative experiments: we tested learning rates of 0.01, 0.001, and 0.0001, finding that 0.0001 achieved optimal model performance, which aligns with literature suggesting that smaller learning rates help models better learn feature representations [39]. The LSTM hidden layer size was determined through multiple rounds of testing, with experimental results showing that when the hidden layer size is too small, diagnostic accuracy is low, while increasing it improves performance but correspondingly increases computational complexity; notably, when the hidden layer size exceeds 64, performance improvement becomes minimal, leading us to set it at 64 considering the optimal balance between computational complexity and performance. In summary, the finalized hyperparameter specifications are detailed in Table 3.

4. Result

In this study, a 0.5s time window was chosen to segment the EEG signals, dividing the EEG data from each subject into individual samples. The training, validation, and test sets were balanced, and 5-fold random cross-validation was used to validate the STTCNN model. Additionally, patients and control groups matched for age and gender participated in this study, with an equal number of evaluations conducted for standard, target, and novel conditions, thus eliminating the possibility of bias between the categories. Furthermore, since the two groups of drugs may exhibit similar trends, for the validation purposes, our pattern recognition experiment was divided into two categories.

In Experiment 1 (CTL vs. PD OFF), all experimental data were obtained from the CTL group and the PD OFF group. According to the grouping numbers in the dataset details in the Appendix A, the dataset was divided into 5 subsets, with 4 subsets selected as the training set in each round and the remaining 1 subset used as the validation set. In Experiment 2 (CTL vs. PD ON), all experimental data were obtained from the CTL group and the PD ON group, and the specific steps were similar to those in Experiment 1.

4.1. Classification performance

By testing on the PD auditory Oddball data, the average accuracy for all experiments in Experiment 1 and Experiment 2 was calculated, and the results are shown in Table 4.

These results are visualized in the form of a histogram in Fig. 5.

The experimental results indicate that the recognition accuracy in Experiment 1 is higher than in Experiment 2. The standard deviation in Experiment 1 is relatively lower than in Experiment 2. This may be

Table 3
Parameter settings.

Layer(type)	Param
learning_rate	0.0001
batch_size	32
epoch	50
weight_decay	0.0001
lstm hidden layer	64

Table 2
Confusion matrix.

Confusion matrix		Predicted label	
		CTL	PD
True Label	CTL	TP	FN
	PD	FP	TN

Table 4
STTCNN classification performance.

Experiment	STTCNN classification performance metrics results				
	Accuracy	F1-score	Recall	Precision	Kappa
Experiment1	92.11	92.00	92.54	91.47	84.08
Experiment2	91.20	90.60	89.98	91.23	82.25

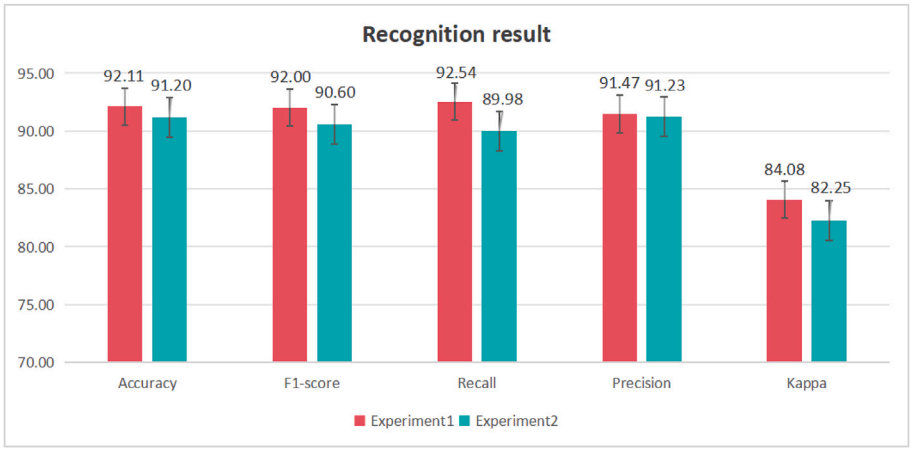

Fig. 5. All subjects in experiment 1 and experiment 2 identified the statistical mean and standard deviation of the results five times. The error bar indicates the standard error.

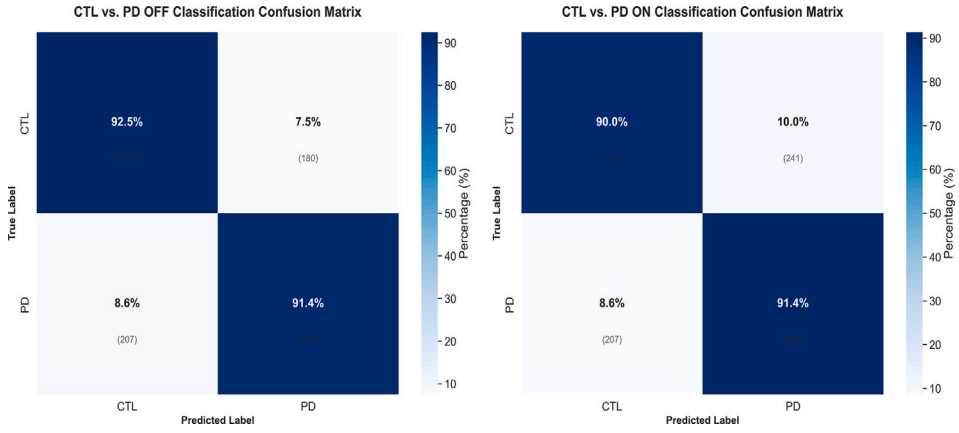

(a) Experiment 1 Confusion matrix (b) Experiment 2 Confusion matrix

Fig. 6. Confusion matrix for experiment 1 and experiment 2.

because patients who are on medication experience some degree of improvement, which reduces the feature differences between the PD ON group and the CTL group, making the classification boundary more ambiguous. As a result, the model has difficulty distinguishing between the two classes, leading to a decrease in accuracy in Experiment 2. This result is also consistent with previous research [27]. The results of the confusion matrix are shown in Fig. 6.

From these, it can be seen that our model achieved good performance when classifying the PD auditory Oddball dataset.

4.2. Comparison with existing methods

The paper collected models for Parkinson's disease recognition and classification from recent years and compared them with the method proposed in this paper. Due to differences in the methods used, sample sizes, channels, and training/testing protocols in the studies, it is challenging to assess the effectiveness of various methods solely based on classification accuracy. Nonetheless, by considering the above-listed metrics, the relative advantages and disadvantages of different approaches can be partially compared.

The comparison results of existing state-of-the-art (SOTA) methods with our method are presented in Table 5. In this table, CV represents cross-validation; TVS refers to Two Validation Strategies (TVS): first, 10-fold cross-validation with all the data; second, 20 % of the training data was also used for validation at the end of each epoch; LPOCV refers to Leave-Pair-Out Cross-Validation; LOCV refers to Leave-One-Out Cross-Validation; KNN refers to K-Nearest Neighbor.

As shown in Table 5, our method outperforms all other methods in terms of accuracy. It should be noted that while our method demonstrates superior performance compared to these publicly reported benchmark methods, the studies corresponding to these reference methods (e.g., CNN, ASGCNN, SVM) employed dissimilar datasets, EEG channel numbers, and experimental protocols—such as differences in data collection paradigms, preprocessing workflows, and model evaluation strategies—which may limit the absolute fairness of cross-study performance comparisons. To conduct a fair comparison, we implemented and present results from SVM [32], EEGNet [41], KNN [42], Random Forest [45], CTESM [46], EEG-GNN [47] and ASGCNN [27], under the same experimental design consisting of identical data, channel numbers, and protocols as the proposed STTCNN in Table 6 and Fig. 7.

Based on the comprehensive experimental results presented in Table 6 and Fig. 7, STTCNN achieved superior performance across both experimental conditions. In Experiment 1, STTCNN attained the highest accuracy of 92.11 % and F1-score of 92.00 %, while in Experiment 2, it achieved 91.20 % accuracy and 90.60 % F1-score, substantially outperforming all baseline methods. Notably, STTCNN demonstrated significant improvements over both traditional machine

Table 5
Comprehensive comparison between existing sota methods and the proposed methods.

Method	Subject	Sampling rate (Hz)	Channel	Protocol	Accuracy(%)
CNN [40]	(20,20)	128	14	TVS	88.25
Logistic Regression [41]	(50,41)	500	214	10-fold CV	56.00
SVM [41]	(50,41)	500	214	10-fold CV	74.70
J48 decision trees [41]	(50,41)	500	214	10-fold CV	68.00
Random Forest [41]	(50,41)	500	214	10-fold CV	78.00
KNN [42]	(118,-)	512	122	5-fold CV	88.00
SVM [42]	(118,-)	512	122	5-fold CV	84.00
SVM [32]	(25,25)	500	60	LPOCV	82.00
LEAPD [43]	(27,27)	500	62	5-fold CV	85.40
Gradient Boosting [44]	(27,27)	500	62	9-fold LOCV	89.30
ASGCNN [27]	(24,24)	500	60	LPOCV	87.67
STTCNN(Ours)	(24,24)	128	60	5-fold CV	**92.11**

Table 6
Average accuracy (%) and F1-score of the baseline methods under the same conditions.

Method	Experiment1		Experiment2	
	Accuracy(%)	F1-score(%)	Accuracy(%)	F1-score(%)
SVM [32]	58.69*	44.12	55.88*	35.12
EEGNet [41]	58.62*	49.77	54.22*	16.17
KNN [42]	63.10*	62.48	61.48*	61.32
Random Forest [45]	61.88*	59.08	60.08*	55.66
CTESM [46]	83.38*	85.84	78.96*	82.80
EEG-GNN [47]	75.02*	73.32	72.50*	73.49
ASGCNN [27]	87.67*	88.41	79.69*	75.52
STTCNN	**92.11**	**92.00**	**91.20**	**90.60**

p-value between the method and STTCNN * indicates ($p < 0.0001$).

learning approaches SVM, KNN, Random Forest and state-of-the-art deep learning methods EEGNet, EEG-GNN, CTESM, ASGCNN. Statistical analysis confirmed that all performance differences between STTCNN and the baseline models were highly significant ($p < 0.0001$), demonstrating the robustness and reliability of the proposed method's improvements. These results validate that STTCNN exhibits comprehensive superiority in terms of accuracy, F1-score, and consistency across different experimental conditions, establishing its effectiveness for EEG-based classification tasks under identical experimental protocols.

4.3. Ablation studies

To validate the effectiveness of the topology mechanism and spatio-temporal feature extractor proposed in STTCNN, we conducted an ablation study to assess the effectiveness of the main building blocks of the proposed framework: the topology arrangement mechanism, temporal branch, spatial branch, and LSTM-based spatio-temporal feature fusion block. The naming and descriptions of each model in this study are shown in Table 7.

Table 7
Names and descriptions of different models in ablation studies.

Model	Description
M_0	Complete structural model
M_1	Electrode topological block not used
M_2	Temporal branch not used
M_3	Spatial branch not used
M_4	Spatio-temporal feature fusion module not used

Fig. 8 shows the experimental results of the ablation study on the PD auditory Oddball dataset for each model. Clearly, in both Experiment 1 and Experiment 2, the full structure achieves higher average classification accuracy than the other structural models, indicating that the synergistic effect of the four key modules significantly enhances classification performance. In contrast, model M_4 performs the worst in both experiments, suggesting that simply using spatio-temporal feature extraction and fusion is insufficient to fully capture the disease-related discriminative features.

Additionally, the accuracy of model M_1 is lower than M_0 in both experiments, further confirming the crucial role of the topology arrangement mechanism in extracting deeper and finer-grained spatio-temporal features. Meanwhile, the accuracy of models M_2 and M_3 is also lower than M_0, indicating the limitations of models relying solely on temporal or spatial features, which may overlook critical details in the EEG signals. It is worth noting that in Experiment 2, the performance of all models is lower than in Experiment 1, likely because after medication,

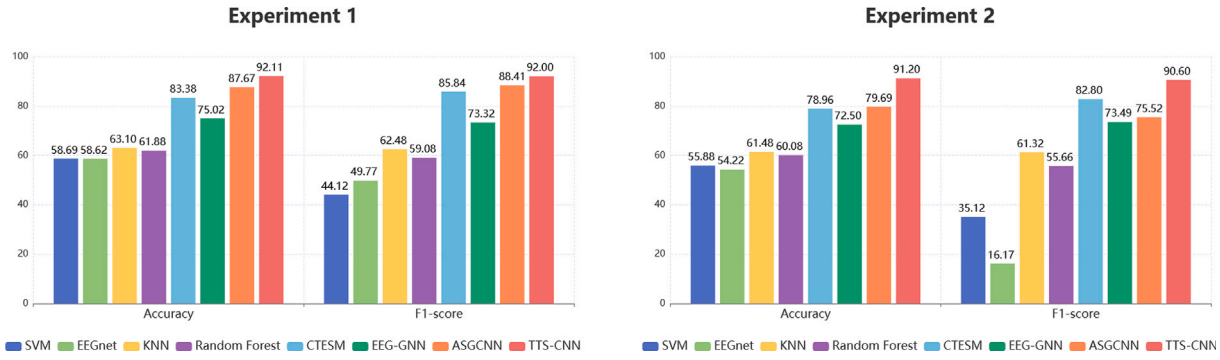

(a) Experiment 1 result of comparision experiment

(b) Experiment 2 result of comparision experiment

Fig. 7. Average accuracy (%) and F1-score of the baseline method under the same conditions.

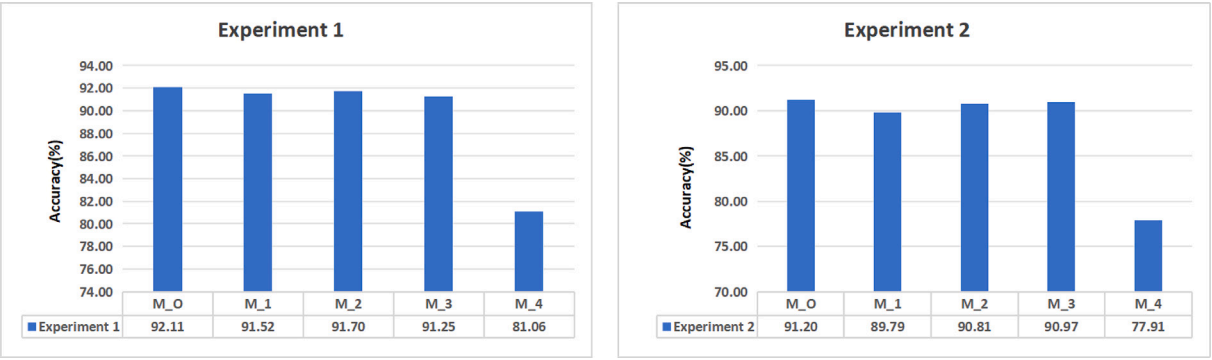

(a) Experiment 1 results of ablation experiment

(b) Experiment 1 results of ablation experiment

Fig. 8. Experimental results of each module under different experiments.

patients show symptom improvement, causing their EEG features to resemble those of healthy individuals, thus increasing the classification difficulty. This further validates the effectiveness of the topology arrangement mechanism, the extraction of spatio-temporal features from branches, and the LSTM-based fusion of spatio-temporal features in the recognition of Parkinson's disease.

5. Discussion

5.1. Analysis of the results of comparative experiments

The comprehensive comparison in Table 5 demonstrates that our proposed STTCNN method achieves superior performance with 92.11 % accuracy despite significant variations in experimental settings across different studies. The performance differences can be attributed to multiple factors:

First, traditional methods such as Logistic Regression [41], J48 decision trees [41], SVM [41], and Random Forest [41] struggle to achieve satisfactory recognition rates, indicating that these methods fail to capture effective electrode selection and intrinsic connectivity relationships between channels. While advanced methods such as ASGCNN [27] and Gradient Boosting [44] incorporate graph-based spatial modeling and ensemble strategies respectively, they still fall short of STTCNN. This demonstrates that the STTCNN model proposed in this paper explicitly models temporal dynamics and spatial correlations through dedicated convolutional modules, achieving more comprehensive feature representation that captures the complex spatiotemporal patterns characteristic of Parkinson's disease EEG signals.

Second, for the same SVM method, we observe dramatically different results: 74.7 % and 84 %, suggesting that experimental protocol selection is crucial for accurate performance assessment. Methods employing specialized protocols such as LPOCV (ASGCNN [27]) or 9-fold LOCV (Gradient Boosting [44]) may not provide fair comparison baselines due to their unique validation characteristics. In contrast, the LEAPD [43] method using standard 5-fold cross-validation achieves 85.4 %, providing a more reliable comparison point. Notably, when compared with algorithms using similar protocols, the STTCNN proposed in this paper consistently demonstrates superior performance, achieving 92.11 % with 5-fold cross-validation, confirming the advantages of this architecture across different evaluation strategies.

Third, while KNN [42] achieves a high accuracy of 88 % with an extensive dataset of 118 subjects, and CNN [40] obtains 88.25 % accuracy using a Two Validation Strategy (TVS) on 20 + 20 subject pairs, both methods demonstrate limitations in their respective architectures. KNN requires broader electrode density to detect PD, which hinders its clinical portability. The CNN's TVS approach, where 20 % of training data is reserved for validation at each epoch, represents a reasonable regularization strategy; however, its performance results suggest that the architecture may not fully exploit the spatiotemporal patterns of EEG signals. The STTCNN proposed in this paper achieves 92.11 % accuracy with 24 + 24 subject pairs, demonstrating that sophisticated spatiotemporal feature learning can extract more informative features from moderate-sized datasets. This suggests that while larger datasets are generally beneficial, architectural innovations in spatiotemporal dynamics modeling may be more impactful than dataset scale alone in EEG-based Parkinson's disease recognition.

Table 6 presents a fair comparison under identical experimental conditions, revealing clear architectural advantages of STTCNN over baseline methods. Traditional machine learning approaches (SVM [32], KNN [42], Random Forest [45]) achieve accuracies below 64 %, possibly due to their over-reliance on handcrafted features that fail to capture complex spatiotemporal dynamics in EEG signals, particularly SVM's [32] linear or simple kernel functions struggling with non-stationary, nonlinear biosignals. Among deep learning methods, EEGNet's [41] performance inferior to STTCNN may be attributed to its lightweight architecture prioritizing interpretability over feature extraction capability, while EEG-GNN [47] may be limited by predefined graph structures that inadequately model dynamic spatiotemporal correlations. Furthermore, to compare with the latest methods, this study introduces CTESM [46] and ASGCNN [27], where the former integrates CNN, transformer and other modules to form a complementary synergistic architecture, and the latter combines sparse graph convolution with attention mechanisms to better capture inter-electrode correlations. However, both methods fall 5–9 percentage points short of STTCNN under identical experimental conditions, suggesting that ASGCNN [27] may lack sufficient attention to the temporal dimension, while CTESM's feature-level attention may insufficiently address joint spatiotemporal modeling problems. In summary, the selection of these baseline models is primarily to ensure comprehensive evaluation coverage. Among these models, traditional machine learning methods represent classical pattern recognition, EEGNet [41] exemplifies EEG-specific lightweight deep models, EEG-GNN [47] demonstrates graph neural network applications, while CTESM [46] and ASGCNN [27] represent state-of-the-art transformer and graph attention-based approaches. The highly significant performance improvements ($p < 0.0001$) statistically further confirm STTCNN's superiority and robustness in Parkinson's disease EEG recognition tasks.

Additionally, to further explore the model's sensitivity to medication effects in Parkinson's disease, we conducted classification experiments between PD ON and PD OFF states. As shown in Table 8, STTCNN achieved an accuracy of 87.29 % with an F1-score of 87.32 % for medication state classification.

The ability to distinguish between ON and OFF medication states is clinically significant, as it could enable objective monitoring of medication effectiveness and timing. The moderate performance (compared

Table 8
STTCNN classification performance.

Experiment	STTCNN classification performance metrics results				
	Accuracy	F1-score	Recall	Precision	Kappa
Experiment3	87.29	87.32	88.61	86.07	74.59

Table 9
The average positive contribution and negative contribution of each brain region.

Brain region	Positive contribution	Negative contribution
Frontal Region	1.83	−0.88
Frontotemporal Region	0.49	−0.53
Central Region	0.70	−0.38
Parietal Region	0.77	−0.98
Occipital Region	1.34	−2.21

to PD vs. Control classification) reflects the subtle neurophysiological differences between medication states, suggesting that EEG-based medication state classification remains challenging but feasible with appropriate deep learning architectures.

5.2. Cerebral regional contributions

In this section, we use SHAP values in conjunction with neural mechanisms and cognitive science of brain Parkinson's disease recognition to explore the importance of different brain regions in our algorithm's prediction of disease classification. SHAP values are based on Shapley values from game theory, which decompose a model's prediction into the contribution of each input feature to the prediction result. By calculating the average SHAP value of the electrodes within each brain region, we can show the positive or negative impact of different brain regions on the prediction result, thereby helping us interpret each brain region's contribution to the model's predictions, enhancing the model's interpretability and transparency, and exploring potential biomarkers for Parkinson's disease recognition.

We input EEG data $D \in R^{N\times C\times T}$ into the trained model, where N is the sample size, C is the number of electrodes, and T is the number of time points. The first 100 segments were taken as baseline data, and 32 segments were randomly selected to calculate the Shap values for each electrode. After obtaining the Shap values for each electrode, the contribution of each brain region was determined by averaging the Shap values of all electrodes within each brain region according to the division of brain regions. The calculated positive and negative contributions of each brain region are shown in Table 9.

Meanwhile, through visual operation, the percentage graphs of the contribution of each brain region and the brain heat maps under different experiments were obtained, as shown in Fig. 9 and Fig. 10.

We know that the frontal region is associated with higher cognitive functions and motor planning [48]. From Table 9, Fig. 9 and Fig. 10, it can be seen that, whether in Experiment 1 or Experiment 2, the frontal region (Frontal Region) consistently has the largest contribution compared to other brain regions, showing strong positivity. This indicates that the frontal region plays the most important role in the disease classification of Parkinson's auditory oddball tasks, which not only highlights the potential of the frontal region in PD auditory dysfunction but also aligns with research in [49,50].

The frontal region's dominant positive contribution (1.83) aligns closely with established PD pathophysiology. The frontal cortex receives substantial dopaminergic innervation from the substantia nigra, and the progressive degeneration of dopaminergic neurons in PD leads to altered frontal cortex activity, manifesting as executive dysfunction and attention deficits [51]. The consistent high contribution across both

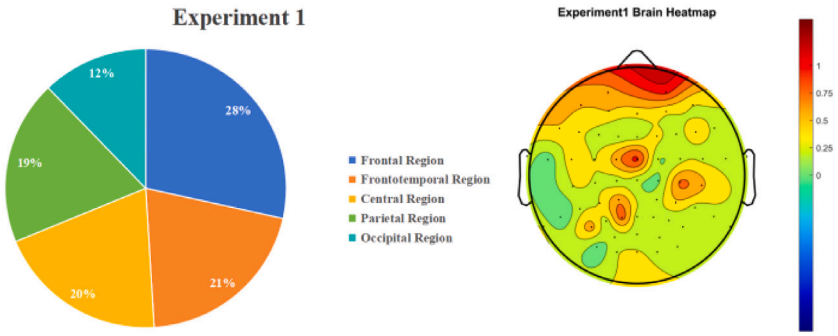

Fig. 9. Experiment 1 Brain area proportion and brain heat map.

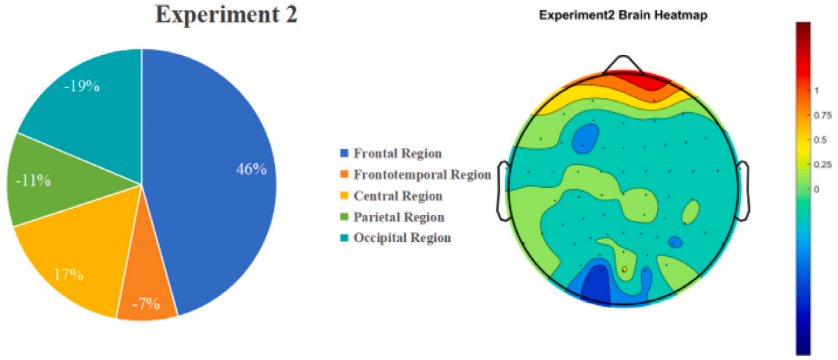

Fig. 10. Experiment 2 Brain area proportion and brain heat map.

experiments suggests that frontal EEG signatures reflect these underlying dopaminergic deficits, making this region a robust neurophysiological marker for PD detection.

Next is the central and frontotemporal regions, which are primarily responsible for functions such as motor control and auditory processing [52]. From Table 9, these regions also contribute significantly to PD recognition, suggesting they are crucial for classifying Parkinson's disease patients. The central region's moderate positive contribution (0.70) reflects its role in sensorimotor processing, which is disrupted in PD due to basal ganglia-thalamocortical circuit dysfunction [53]. Notably, the frontotemporal contribution decreased in Experiment 2, possibly because this region's function improved after medication, consistent with previous research [54]. This pattern suggests that frontotemporal EEG signatures could serve as objective markers for assessing medication efficacy.

The parietal and occipital regions show weaker positive contributions despite substantial negative contributions, requiring careful interpretation. The parietal cortex receives less direct dopaminergic innervation compared to frontal regions, and parietal dysfunction typically manifests in advanced PD stages [55]. The occipital region's mixed contribution pattern likely reflects preserved visual processing in early-to-moderate PD, where primary sensory functions remain intact [56]. The negative contributions suggest that normal activity patterns in these regions may indicate healthy functioning.

The dominance of frontal region signatures suggests that EEG-based PD assessment could be implemented using targeted electrode montages focused on frontal areas, reducing complexity and improving feasibility. The current findings suggest that a frontal contribution ratio >60 % combined with reduced parietal/occipital involvement could serve as diagnostic criteria. The medication-sensitive frontotemporal patterns could inform personalized treatment approaches, helping clinicians optimize dopaminergic therapy.

These findings demonstrate that different brain regions contribute distinctly to PD recognition, with frontal dominance reflecting core pathophysiological changes, moderate central/frontotemporal involvement indicating medication-sensitive processes, and weak parietal/occipital contributions confirming the specificity of disease-related neural signatures. This regional analysis enhances model interpretability and provides a neurobiological foundation for developing clinically relevant EEG biomarkers for PD diagnosis and monitoring.

6. Conclusion

This study proposes a Spatio-Temporal Topological Convolutional Neural Network (STTCNN) that enhances EEG spatial representation through electrode spatial reorganization, combines temporal periodicity modeling with progressive spatial convolution for multi-scale feature extraction, and utilizes LSTM for dynamic fusion. The research demonstrates that topological awareness in neural network architectures is essential for robust EEG-based neurological analysis, revealing that spatial encoding aligned with brain anatomy represents a fundamental paradigm shift from traditional data-driven methods. The findings indicate that topological neural networks represent a necessary evolution toward clinically meaningful EEG analysis, where spatial organization reflects underlying brain connectivity with profound implications for neurological diagnostic systems. Clinically, this study provides compelling evidence that anatomically-based approaches significantly enhance diagnostic reliability and offer practical advantages for EEG-based diagnosis. Although the spatial reorganization and feature extraction framework is theoretically applicable to other EEG paradigms, systematic validation across different protocols can still be further explored. Future work should prioritize validation on larger, more diverse datasets through phased strategies from single-center to multi-center studies, extend evaluation to other EEG paradigms to establish broader clinical utility, and ultimately bridge neuroscientific understanding with clinical practice.

Table 10
Database sample details.

No.	CTL			PD			
	Sex	Age	ID	Sex	Age	ON ID	OFF ID
1	Female	83	8060	Male	75	804–1	804–2
2	Female	67	8070	Male	79	805–1	805–2
3	Female	66	890	Female	79	806–2	806–1
4	Male	80	891	Female	72	807–2	807–1
5	Female	64	892	Male	68	808–2	808–1
6	Female	64	893	Male	71	809–1	809–2
7	Male	58	896	Male	68	811–1	811–2
8	Male	70	897	Male	83	813–2	813–1
9	Male	64	898	Male	61	814–1	814–2
10	Male	52	899	Male	55	815–1	815–2
11	Male	84	900	Female	49	816–2	816–1
12	Female	69	901	Male	71	817–2	817–1
13	Male	83	902	Female	74	818–1	818–2
14	Male	83	903	Male	76	819–2	819–1
15	Male	73	904	Male	72	820–1	820–2
16	Female	58	905	Female	49	821–1	821–2
17	Male	77	906	Male	70	822–1	822–2
18	Female	65	907	Female	64	823–2	823–1
19	Male	64	909	Male	78	824–2	824–1
20	Male	75	910	Female	77	825–1	825–2
21	Male	73	911	Male	66	826–1	826–2
22	Male	75	912	Male	68	827–2	827–1
23	Male	69	913	Female	76	828–2	828–1
24	Female	48	914	Female	73	829–2	829–1
SUM	F/M 9/15	mean/std 69/9.78	24	F/M 9/15	mean/std 69.75/8.91	24	24

CRediT authorship contribution statement

Weixiang Gao: Writing – review & editing, Writing – original draft, Visualization, Validation, Supervision, Software, Resources, Project administration, Methodology, Investigation, Funding acquisition, Formal analysis, Data curation, Conceptualization. **Yunyuan Gao:** Writing – review & editing, Supervision, Resources, Project administration, Investigation, Funding acquisition, Data curation. **Jiangwen Lu:** Writing – review & editing, Validation, Project administration. **Xugang Xi:** Project administration, Funding acquisition, Data curation. **Xiaohui Lou:** Resources, Data curation.

Declaration of competing interest

The authors declare that they have no known competing financial interests or personal relationships that could have appeared to influence the work reported in this paper.

Acknowledgement

This work was supported in part by the National Natural Science Foundation of China (62371171, 62371178, 62271181), and the Zhejiang Provincial Natural Science Foundation of China (LZ25F010006).

Appendix A

Table 10 presents detailed demographic characteristics of all study participants. This table validates the scientific rigor of our study design: the control and PD groups achieved good matching in age and sex, eliminating the potential impact of these important confounding factors on EEG classification results. Additionally, the table demonstrates that each PD patient completed EEG recordings under both ON and OFF medication states. This dual-state design provides an important foundation for comprehensive understanding of neurophysiological changes in Parkinson's disease.

Data availability

Data will be made available on request.

References

[1] S. Ramesh, A.S.P. Molligoda Arachchige, Depletion of dopamine in parkinson's disease and relevant therapeutic options: a review of the literature, AIMS Neurosci. 10 (3) (2023) 200–231, https://www.aimspress.com/article/doi/10.3934/Neuroscience.2023017.

[2] S. Jones, K.M. Torsney, L. Scourfield, K. Berryman, E.J. Henderson, Neuropsychiatric symptoms in parkinson's disease: aetiology, diagnosis and treatment, BJPsych Adv. 26 (6) (2020) 333–342, https://doi.org/10.1192/bja.2019.79.

[3] D.M. Radhakrishnan, V. Goyal, Parkinson's disease: a review, Neurol. India 66 (Suppl 1) (2018) S26–S35, https://doi.org/10.4103/0028-3886.226451.

[4] K. Berganzo, B. Tijero, A. González-Eizaguirre, J. Somme, E. Lezcano, I. Gabilondo, M. Fernandez, J.J. Zarranz, J.C. Gómez-Esteban, Motor and non-motor symptoms of parkinson's disease and their impact on quality of life and on different clinical subgroups, Neurol (Engl. Ed.) 31 (9) (2016) 585–591, https://doi.org/10.1016/j.nrleng.2014.10.016.

[5] G. Santangelo, C. Vitale, M. Picillo, M. Moccia, S. Cuoco, K. Longo, D. Pezzella, A. di Grazia, R. Erro, M.T. Pellecchia, et al., Mild cognitive impairment in newly diagnosed parkinson's disease: A longitudinal prospective study, Parkinsonism Relat. Disord. 21 (10) (2015) 1219–1226, https://doi.org/10.1016/j.parkreldis.2015.08.024.

[6] E. Mulroy, R. Erro, K.P. Bhatia, M. Hallett, Refining the clinical diagnosis of parkinson's disease, Parkinsonism Relat. Disord. 122 (2024) 106041, https://doi.org/10.1016/j.parkreldis.2024.106041.

[7] G. AlMahadin, A. Lotfi, E. Zysk, F.L. Siena, M. Mc Carthy, P. Breedon, Parkinson's disease: current assessment methods and wearable devices for evaluation of movement disorder motor symptoms - a patient and healthcare professional perspective, BMC Neurol. 20 (1) (2020) 419, https://doi.org/10.1186/s12883-020-01996-7.

[8] X. Li, C. Chen, T. Pan, X. Zhou, X. Sun, Z. Zhang, D. Wu, X. Chen, Trends and hotspots in non-motor symptoms of parkinson's disease: A 10-year bibliometric analysis, Front. Aging Neurosci. 16 (2024) 1335550, https://doi.org/10.3389/fnagi.2024.1335550.

[9] M. Dauwan, J.I. Hoff, E.M. Vriens, A. Hillebrand, C.J. Stam, I.E. Sommer, Aberrant resting-state oscillatory brain activity in parkinson's disease patients with visual hallucinations: An meg source-space study, neuroimage: Clin. 22 (2019) 101752, https://doi.org/10.1016/j.nicl.2019.101752.

[10] Y. Song, J. Xu, A.T. Agbele, Advancements in ultrasonography and mri for enhanced diagnosis of parkinson's disease: An updated review, J. Radiat. Res. Appl. Sci. 17 (3) (2024) 101015, https://doi.org/10.1016/j.jrras.2024.101015.

[11] F. Cieri, P.P. Giriprakash, R. Nandy, X. Zhuang, R.L. Doty, J.Z.K. Caldwell, D. Cordes, Functional connectivity differences of the olfactory network in parkinson's disease, mild cognitive impairment and cognitively normal individuals: A resting-state fmri study, Neuroscience 559 (2024) 8–16, https://doi.org/10.1016/j.neuroscience.2024.08.031.

[12] E. Yıldırım, T. Aktürk, L. Hanoğlu, G. Yener, C. Babiloni, B. Güntekin, Lower oddball event-related eeg delta and theta responses in patients with dementia due to parkinson's and lewy body than alzheimer's disease, Neurobiol. Aging 137 (2024) 78–93, https://doi.org/10.1016/j.neurobiolaging.2024.02.004.

[13] P. Pradeep, J. Kamalakannan, Comprehensive review of literature on parkinson's disease diagnosis, Comput. Biol. Chem. 113 (2024) 108228, https://doi.org/10.1016/j.compbiolchem.2024.108228.

[14] F.I. Alanazi, T.M. Al-Ozzi, S.K. Kalia, et al., Neurophysiological responses of globus pallidus internus during the auditory oddball task in parkinson's disease, Neurobiol. Dis. 159 (2021) 105490, https://doi.org/10.1016/j.nbd.2021.105490.

[15] A. Droby, S. Nosatzki, Y. Edry, et al., The interplay between structural and functional connectivity in early stage parkinson's disease patients, J. Neurol. Sci. 442 (2022) 120452, https://doi.org/10.1016/j.jns.2022.120452.

[16] L. Qiu, J. Li, L. Zhong, W. Feng, C. Zhou, J. Pan, A novel eeg-based parkinson's disease detection model using multiscale convolutional prototype networks, IEEE Trans. Instrum. Meas. 73 (2024) 1–14, https://doi.org/10.1109/TIM.2024.3351248.

[17] J. Li, X. Li, Y. Mao, J. Yao, J. Gao, X. Liu, Classification of parkinson's disease eeg signals using 2d-mdagts model and multi-scale fuzzy entropy, Biomed. Signal Process. Control 91 (2024) 105–872, https://doi.org/10.1016/j.bspc.2023.105872.

[18] C. Chu, Z. Zhang, J. Wang, Z. Li, X. Shen, X. Han, L. Bai, C. Liu, X. Zhu, Temporal and spatial variability of dynamic microstate brain network in early parkinson's disease, NPJ Parkinsons Dis. 9 (2023) 57, https://doi.org/10.1038/s41531-023-00498-w.

[19] C. Neves, Y. Zeng, Y. Xiao, Parkinson's disease detection from resting state eeg using multi-head graph structure learning with gradient weighted graph attention explanations, Vol. 15266, Springer, Cham, 2025, pp. 3–12, https://doi.org/10.1007/978-3-031-78761-4_1.

[20] Z. Wang, S. Li, X. Chen, et al., Time-frequency transform based eeg data augmentation for brain-computer interfaces, Knowl. Based Syst. (2025) 113074 https://doi.org/10.1016/j.knosys.2025.113074.

[21] J.W. Li, G.Y. Feng, J.J. Lv, R.J. Chen, L.J. Wang, X.X. Zeng, J. Yuan, X.L. Hu, H.M. Zhao, X. Lu, A rhythmic encoding approach based on eeg time-frequency image for epileptic seizure detection, Biomed. Signal Process. Control 99 (2025) 106824, https://doi.org/10.1016/j.bspc.2024.106824.

[22] Y. Wei, Y. Liu, C. Li, J. Cheng, R. Song, X. Chen, Tc-net: A transformer capsule network for eeg-based emotion recognition, Comput. Biol. Med. 152 (2023) 106463, https://doi.org/10.1016/j.compbiomed.2022.106463.

[23] N. Sharma, A. Upadhyay, M. Sharma, et al., Deep temporal networks for eeg-based motor imagery recognition, Sci. Rep. 13 (1) (2023) 18813, https://doi.org/10.1038/s41598-023-41653-w.

[24] H. Wu, T. Hu, Y. Liu, H. Zhou, J. Wang, M. Long, Timesnet: Temporal 2d-variation modeling for general time series analysis, arXiv preprint arXiv:2210.02186https://doi.org/10.48550/arXiv.2210.02186 (2022).

[25] T. Zhang, X. Wang, X. Xu, et al., Gcb-net: Graph convolutional broad network and its application in emotion recognition, IEEE Trans. Affect. Comput. 13 (1) (2019) 379–388, https://doi.org/10.1109/taffc.2019.2937768.

[26] J. Zhou, X. Zhang, Z. Jiang, Recognition of imbalanced epileptic eeg signals by a graph-based extreme learning machine, Wirel. Commun. Mob. Comput. 2021 (1) (2021) 5871684, https://doi.org/10.1155/2021/5871684.

[27] H. Chang, B. Liu, Y. Zong, et al., Eeg-based parkinson's disease recognition via attention-based sparse graph convolutional neural network, IEEE J. Biomed. Health Inform. 27 (11) (2023) 5216–5224, https://doi.org/10.1109/jbhi.2023.3292452.

[28] L. Han, X. Zhang, J. Yin, Eeg emotion recognition based on the timesnet fusion model, Appl. Soft Comput. 159 (2024) 111635, https://doi.org/10.1016/j.asoc.2024.111635.

[29] Y. Zhang, J. Qu, Q. Zhang, C. Cheng, Eeg-based emotion recognition based on 4d feature representations and multiple attention mechanisms, Biomed. Signal Process. Control 103 (2025) 107432, https://doi.org/10.1016/j.bspc.2024.107432.

[30] Z. Chen, R. Yang, M. Huang, F. Li, G. Lu, Z. Wang, Eegprogress: A fast and lightweight progressive convolution architecture for eeg classification, Comput. Biol. Med. 169 (2024) 107901, https://doi.org/10.1016/j.compbiomed.2023.107901.

[31] Y. Yin, X. Zheng, B. Hu, Y. Zhang, X. Cui, Eeg emotion recognition using fusion model of graph convolutional neural networks and lstm, Appl. Soft Comput. 100 (2021) 106954, https://doi.org/10.1016/j.asoc.2020.106954.

[32] J.F. Cavanagh, P. Kumar, A.A. Mueller, S.P. Richardson, A. Mueen, Diminished eeg habituation to novel events effectively classifies parkinson's patients, Clin. Neurophysiol. 129 (2) (2018) 409–418, https://doi.org/10.1016/j.clinph.2017.11.023.

[33] H. Nolan, R. Whelan, R.B. Reilly, Faster: Fully automated statistical thresholding for eeg artifact rejection, J. Neurosci. Methods 192 (1) (2010) 152–162, https://doi.org/10.1016/j.jneumeth.2010.07.015.

[34] A. Gu, K. Goel, C. Ré, Efficiently modeling long sequences with structured state spaces, arXiv preprint arXiv:2111.00396 https://doi.org/10.48550/arXiv.2111.00396 (2021).

[35] T. Zhou, Z. Ma, Q. Wen, X. Wang, L. Sun, R. Jin, Fedformer: Frequency enhanced decomposed transformer for long-term series forecasting, in: International conference on machine learning, PMLR, 2022, pp. 27268–27286, https://doi.org/10.48550/arXiv.2201.12740.

[36] H. Wu, J. Xu, J. Wang, M. Long, Autoformer: Decomposition transformers with auto-correlation for long-term series forecasting, Adv. Neural Inf. Process. Syst. 34 (2021) 22419–22430, https://doi.org/10.48550/arXiv.2106.13008.

[37] Z.Y. Zhang, Q.H. Meng, L.C. Jin, H.G. Wang, H.R. Hou, A novel eeg-based graph convolution network for depression detection: Incorporating secondary subject partitioning and attention mechanism, Expert Syst. Appl. 239 (2024) 122356, https://doi.org/10.1016/j.eswa.2023.122356.

[38] J. Cohen, A coefficient of agreement for nominal scales, Educ. Psychol. Meas. 20 (1960) 37–46.

[39] C. Cooney, A. Korik, R. Folli, D. Coyle, Evaluation of hyperparameter optimization in machine and deep learning methods for decoding imagined speech eeg, Sensors 20 (16) (2020) 4629, https://doi.org/10.3390/s20164629.

[40] S.L. Oh, Y. Hagiwara, U. Raghavendra, R. Yuvaraj, N. Arunkumar, M. Murugappan, U.R. Acharya, A deep learning approach for parkinson's disease diagnosis from eeg signals, Neural Comput. Appl. 32 (2020) 10927–10933, https://doi.org/10.1007/s00521-018-3689-5.

[41] M. Chaturvedi, F. Hatz, U. Gschwandtner, J.G. Bogaarts, A. Meyer, P. Fuhr, V. Roth, Quantitative eeg (qeeg) measures differentiate parkinson's disease (pd) patients from healthy controls (hc), Front. Aging Neurosci. 9 (2017) 3, https://doi.org/10.3389/fnagi.2017.00003.

[42] N. Betrouni, A. Delval, L. Chaton, L. Defebvre, A. Duits, A. Moonen, A.F.G. Leentjens, K. Dujardin, Electroencephalography-based machine learning for cognitive profiling in parkinson's disease: Preliminary results, Mov. Disord. 34 (2) (2019) 210–217, https://doi.org/10.1002/mds.27528.

[43] M.F. Anjum, S. Dasgupta, R. Mudumbai, A. Singh, J.F. Cavanagh, N.S. Narayanan, Linear predictive coding distinguishes spectral eeg features of parkinson's disease, Parkinsonism Relat. Disord. 79 (2020) 79–85, https://doi.org/10.1016/j.parkreldis.2020.08.001.

[44] S.-B. Lee, Y.-J. Kim, S. Hwang, H. Son, S.K. Lee, K.-I. Park, Y.-G. Kim, Predicting parkinson's disease using gradient boosting decision tree models with electroencephalography signals, Parkinsonism Relat. Disord. 95 (2022) 77–85, https://doi.org/10.1016/j.parkreldis.2022.01.011.

[45] V.J. Lawhern, A.J. Solon, N.R. Waytowich, S.M. Gordon, C.P. Hung, B.J. Lance, Eegnet: A compact convolutional neural network for eeg-based brain–computer interfaces, J. Neural Eng. 15 (5) (2018) 056013, https://doi.org/10.1088/1741-2552/aace8c.

[46] C. Bunterngchit, L.H. Baniata, H. Albayati, M.H. Baniata, K. Alharbi, F.H. Alshammari, S. Kang, A hybrid convolutional-transformer approach for accurate electroencephalography (eeg)-based parkinson's disease detection, Bioeng (Basel) 12 (6) (2025) 583, pMID: 40564400; PMCID: PMC12189856; https://doi.org/10.3390/bioengineering12060583.

[47] A. Demir, T. Koike-Akino, Y. Wang, M. Haruna, D. Erdogmus, Eeg-gnn: Graph neural networks for classification of electroencephalogram (eeg) signals, 2021 43rd Annu. Int. Conf. IEEE Eng. Med. Biol. Soc (EMBC) (2021) 1061–1067https://doi.org/10.1109/EMBC46164.2021.9630194.

[48] C. Heitmann, M. Zhan, M. Linke, C. Hölig, R. Kekunnaya, R. van Hoof, R. Goebel, B. Röder, Early visual experience refines the retinotopic organization within and across visual cortical regions, Curr. Biol. 33 (22) (2023) 4950–4959.e4, https://doi.org/10.1016/j.cub.2023.10.010.

[49] S. Zhu, W. Yi, S. Wang, Q. Wang, D. Bai, W. Liu, J. Wang, Phase slope transfer entropy analysis of eeg in patients with parkinson's disease, Biomed. Signal Process. Control 100 (2025) 107043, https://doi.org/10.1016/j.bspc.2024.107043.

[50] B.N. Jávor-Duray, M. Vinck, M. van der Roest, E. Bezard, H.W. Berendse, T. Boraud, P. Voorn, Alterations in functional cortical hierarchy in hemiparkinsonian rats, J. Neurosci. 37 (32) (2017) 7669–7681, https://doi.org/10.1523/jneurosci.3257-16.2017.

[51] Z. Zhou, Y. Yan, H. Gu, R. Sun, Z. Liao, K. Xue, C. Tang, Dopamine in the prefrontal cortex plays multiple roles in the executive function of patients with parkinson's disease, Neural Regen. Res. 19 (8) (2024) 1759–1767, https://doi.org/10.4103/1673-5374.389631.

[52] Z. Wang, K. Xue, Y. Kang, Z. Liu, J. Cheng, Y. Zhang, Y. Wei, Altered intrinsic neural activity and its molecular analyses in first-episode schizophrenia with auditory verbal hallucinations, Front. Neurosci. 18 (2024) 1478963, https://doi.org/10.3389/fnins.2024.1478963.

[53] M.M. McGregor, A.B. Nelson, Circuit mechanisms of parkinson's disease, Neuron 101 (6) (2019) 1042–1056, https://doi.org/10.1016/j.neuron.2019.03.004.

[54] L. Wang, J. Yao, X. Lv, Y. Xu, W. Dou, H. Zhang, J. Ye, Y.-C. Chen, et al., Characterizing microstructural patterns within the cortico-striato-thalamo-cortical circuit in parkinson's disease, Prog. Neuro-Psychopharmacol. Biol. Psychiatry 135 (2024) 111116, https://doi.org/10.1016/j.pnpbp.2024.111116.

[55] F. Nieto-Escamez, E. Obrero-Gaitán, I. Cortés-Pérez, Visual dysfunction in parkinson's disease, Brain Sci. 13 (8) (2023) 1173, https://doi.org/10.3390/brainsci13081173.

[56] R.A. Armstrong, Oculo-visual dysfunction in parkinson's disease, J. Parkinsons Dis. 5 (4) (2015) 715–726, https://doi.org/10.3233/JPD-150686.